

Comparative Study of Non-Electrochemical Hysteresis Models for LiFePO_4 /Graphite Batteries

Jiachen Ma[†], Jiale Xie^{*}, and Kun Bai^{**}

^{†,*} School of Astronautics, Harbin Institute of Technology, Harbin, China

^{**} Maintenance Branch, State Grid Jibei Electric Power Co. Ltd., Beijing, China

Abstract

The estimation of LiFePO_4 /graphite battery states suffers from the prominent hysteresis phenomenon between the respective open-circuit voltage curves towards charging and discharging. A lot of hysteresis models have been documented to investigate the hysteresis mechanism. This paper reviews and deeply interprets four non-electrochemical hysteresis models and some improvements. These models can be conveniently incorporated into commonly used equivalent circuit models to reproduce battery behaviors. Through simulation and experimental comparisons of voltage predictions and state-of-charge estimations, the pros and cons of these models are presented.

Key words: Hysteresis model, LiFePO_4 battery, Open-circuit voltage, State-of-charge estimation

I. INTRODUCTION

For electric vehicles (EVs), lithium-ion batteries (LiBs) are currently the best tradeoff between energy/power density and mass production cost. Benefiting from a long cycle life, nontoxicity, material commercial accessibility and safety-to-abuse [1], [2], LiFePO_4 -based olivine cathodes have been deemed promising alternatives to rare-metal cathodes, such as LiCoO_2 and LiNiO_2 [3]. In addition, the flat open-circuit voltage (OCV) plateau across the dominant SoC range of LiFePO_4 batteries (LFPBs) [4] can deliver a constant power output for EVs.

Whether as a core relationship to be incorporated into the equivalent circuit models (ECMs), or as a correction manner to recalibrate the coulomb counting results, the OCV-SoC correlation plays an irreplaceable role for SoC estimation [7]-[9]. However, the pronounced OCV-SoC hysteresis phenomenon makes the conventional estimation methods for other battery chemistries inapplicable to LFPBs [5], [6]. As a result, this peculiar OCV-SoC characteristic greatly complicates, and sometimes even disables, the determination of some mandatory indexes, e.g., remaining range and state

of available power [8], [10], for reliable EV operation.

In essence, the actual variable that embodies a one-to-one correspondence to the SoC is the electromotive force (EMF) [11], which denotes the absolute potential between battery electrodes. Due to the immeasurability of EMF, several hours are ordinarily relaxed to measure the OCV, which is used as a substitute for the EMF in practical applications. Nevertheless, there exists no monotonic dependence between OCV and SoC as the EMF-SoC correlation manifests, i.e., the OCV is not solely determined by the SoC but is relevant to charge/discharge pretreatments. Originating from the complex thermodynamic effects and electrode distortions [12], OCV hysteresis is inevitable for most battery chemistries and is especially evident for LFPBs [3], [8], [13], [14]. As illustrated in Fig. 1(a), two separate OCV boundaries, $U_{oc}^{up}(z)$ and $U_{oc}^{low}(z)$, towards charging and discharging, can be acquired on a LiFePO_4 cell, (SoC is abbreviated as z and OCV as U_{oc}). The gap between the boundaries can reach up to 40mV, which is mainly ascribed to hysteresis potential.

During the terminal SoC ranges (0~10% and 95~100%), OCV exhibits neither flatness nor obvious hysteresis, and this steep appearance makes the SoC mapped from OCV-SoC relatively reliable. Meanwhile, over the dominant SoC window (10~95%), OCV characterizes a gentle slope (a large gradient of $d\text{SoC}/dU_{oc}$), which implies that the mapped SoC is sensitive to the input U_{oc} . Therefore, even a small disturbance on U_{oc} leads to a considerable SoC bias [8],

Manuscript received Jan. 19, 2018; accepted May 3, 2018

Recommended for publication by Associate Editor Jonghoon Kim.

[†]Corresponding Author: hitwhrobot@126.com

Tel: +86-13963119266, Harbin Institute of Technology

^{*}School of Astronautics, Harbin Institute of Technology, China

^{**}Maintenance Branch, State Grid Jibei Electric Power Co. Ltd., China

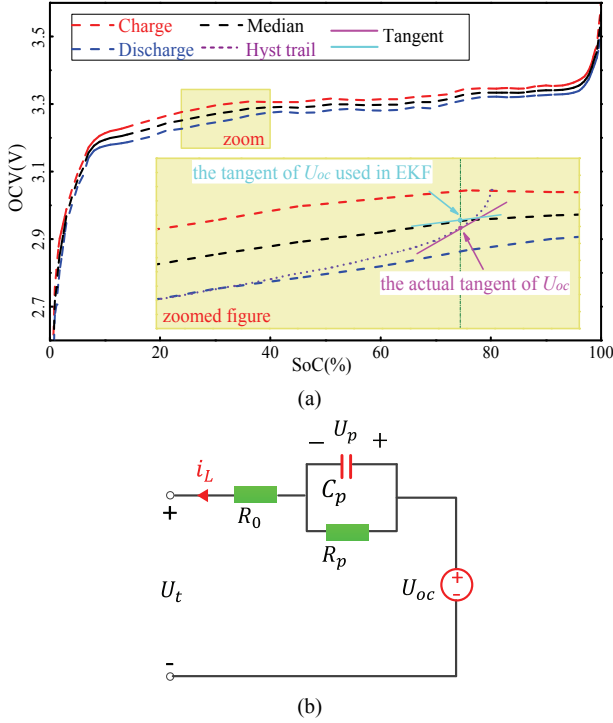


Fig. 1. Mechanism analysis and model introduction of the EKF method: (a) Tangents of the median OCV curve and the actual OCV curve at a given SoC, (b) First-order RC model.

[11], [15], [16]. Unfortunately, electro-magnetic interference and signal drift usually pollute the measured voltage with deviations of up to 5mV, which is also the accuracy grade of most equipment. This results in considerable SoC evaluation errors.

Accordingly, the Extended Kalman filter (EKF) is introduced to suppress system noise and measurement noise. Taking the frequently used first-order ECM in Fig. 1(b) as an example, a set of expressions can be written as:

$$\begin{cases} U_t = U_{oc} - U_p - i_L R_0 \\ \dot{U}_p = \frac{i_L}{C_p} - \frac{U_p}{C_p R_p} \\ U_{oc}(z) = K_0 + K_1 z + K_2/z + K_3 \ln z + K_4 \ln(1-z) \end{cases} \quad (1)$$

Based on Eq. (1), a discrete-time state-space can be obtained as:

$$\begin{cases} X_k = A_{k-1} X_{k-1} + B_{k-1} u_{k-1} + \omega_{k-1} \\ Y_k = h(X_k, u_k) + v_k \end{cases} \quad (2)$$

where $\begin{cases} X_k = [U_{p,k} \quad z_k]^T, Y_k = [U_{t,k}] \\ A_k = \text{diag}([\exp(-\Delta t/\tau) \quad 1]) \\ B_k = [(1 - \exp(-\Delta t/\tau))R_p \quad -\eta\Delta t/C_N]^T, C_N \text{ is} \\ h(X_k, u_k) = U_{oc}(z_k) - U_{p,k} - I_{L,k} R_0 \\ u_k = [i_{L,k}], \tau = R_p C_p \end{cases}$

the rated capacity, η is the coulombic efficiency, k is the step index, and Δt is the sampling interval.

Conventionally, the median curve between $U_{oc}^{up}(z)$ and $U_{oc}^{low}(z)$ is approximated as the EMF by ignoring the

TABLE I
ALGORITHM DETAILS OF THE EXTENDED KALMAN ALGORITHM

State-space expression^a

$$X_k = f(X_{k-1}, u_{k-1}) + \omega_{k-1} \quad (3)$$

$$Y_k = h(X_k, u_k) + v_k \quad (4)$$

Linearization^b

$$F_k = \left. \frac{\partial f}{\partial X} \right|_{\hat{X}_{k,k}}, \quad H_k = \left. \frac{\partial h}{\partial X} \right|_{\hat{X}_{k,k}}$$

Initialization, for $k = 0$

$$\hat{X}_{0,0} = \mathbb{E}(X_{0,0})$$

$$P_{0,0} = \mathbb{E}[(X_{0,0} - \hat{X}_{0,0})(X_{0,0} - \hat{X}_{0,0})^T]$$

For $k = 1, 2, \dots$

$$P_{k,k-1} = F_{k-1} P_{k-1,k-1} F_{k-1}^T + Q_{k-1} \quad (5)$$

$$K_k = P_{k,k-1} H_k^T (H_k^T P_{k,k-1} H_k + R_k)^{-1} \quad (6)$$

$$\hat{X}_{k,k-1} = f(\hat{X}_{k-1,k-1}, u_{k-1}) \quad (7)$$

$$\hat{X}_{k,k} = \hat{X}_{k,k-1} + K_k (Y_k - h(\hat{X}_{k,k-1}, u_k)) \quad (8)$$

$$P_{k,k} = (I - K_k H_k) P_{k,k-1} \quad (9)$$

hysteresis potential [11], [18], [19], i.e. $\text{EMF} = U_{oc}$. Then a simplified electrochemical equation can be used to fit the OCV-SoC correlation [17], e.g. the $U_{oc}(z)$ in Eq. (1). Thereafter, the EKF algorithm in Table I can be operated recursively to obtain the SoC.

However, the performance of EKF primarily relies on the accuracy of the employed battery models, and may suffer divergence issues in the case of strong non-linearity. The existence of hysteresis makes hysteresis-free ECMs low-quality for LFPBs, which hinders the ability of estimating the SoC reliably. The following explanation gives a detailed analysis.

Note 1: Why cannot an EKF estimator based on hysteresis-free ECMs handle the SoC estimation for LFPBs?

The second element of the Jacobian matrix H_k , namely $H_k(1,2) = \partial U_{oc}(z)/\partial z|_{z_k}$, represents the change rate of U_{oc} with respect to the SoC at a specific point \hat{z}_k . It is essentially a local linearity approximation by applying a Taylor expansion on $U_{oc}(z)$ and retaining the first-order term. Then the state-space expression can be transformed into a linear form and Eq. (6) can be operated. When there exists hysteresis potential, the actual change rate of U_{oc} exhibits a large deviation to $H_k(1,2)$ as shown in Fig. 1(a). This noticeable inconsistency leads to an incorrect gain K_k (Eq. (6)), which is used to correct the state estimation $\hat{X}_{k,k}$ (Eq. (8)) and to update the statistical property $P_{k,k}$ (Eq. (9)) for the following recursions. The whole hysteresis process is a long-term transition which can last for a span up to 15% SoC. As a consequence, this discrepancy can easily make the estimation result slip to the SoC ranges with slopes that are close to the actual $\dot{U}_{oc}(z)$. Some simple hysteresis models, such as the zero-state model [20], are also unsuitable since

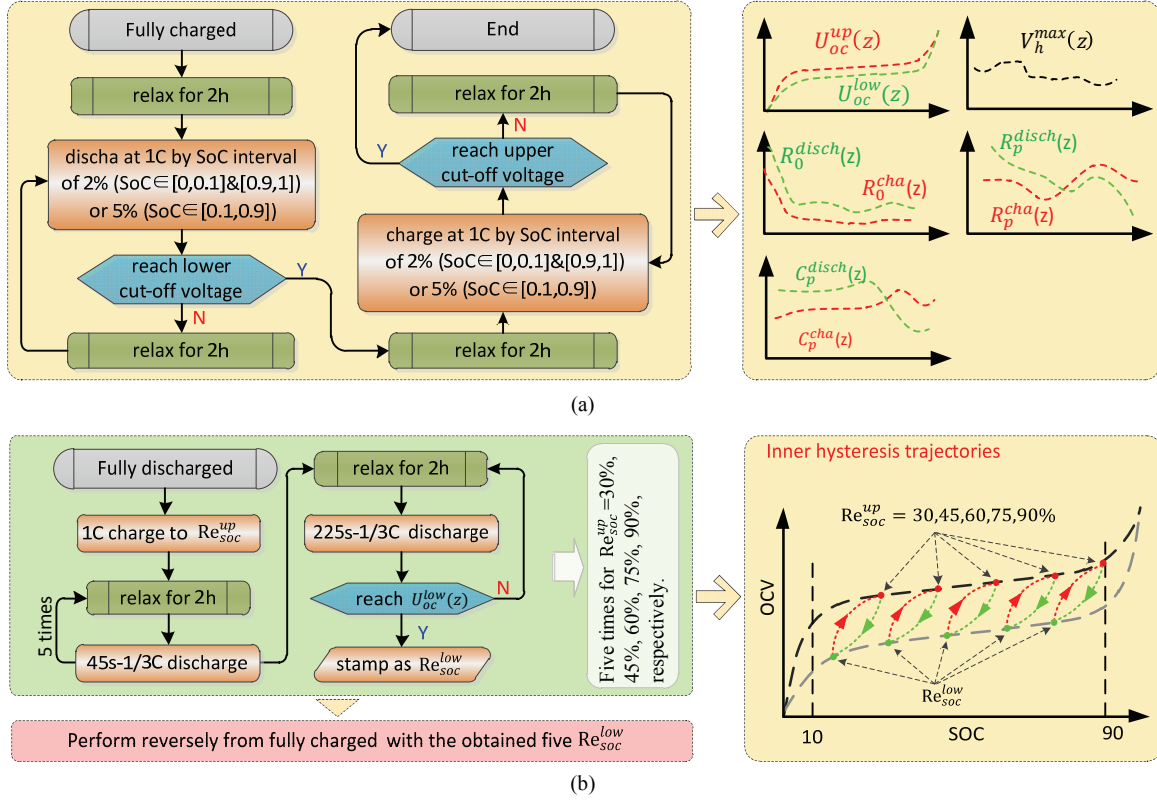


Fig. 2. Characteristic test procedures: (a) Identifying the OCV-SoC correlations and the V_h^{max} , R_0 , R_p and C_p , (b) Acquiring the hysteresis trajectories.

the EKF is designed to deal with stationary stochastic processes, while the zero-state model simplifies the slow hysteresis transition to immediate flip between $U_{oc}^{up}(z)$ and $U_{oc}^{low}(z)$. This would results in drastic oscillations, even divergence, in case of frequent charge/discharge alternations.

Aiming for accurate battery models of LFPBs, the hysteresis potential needs to be encompassed. Though [12], [21] explain the hysteresis mechanism and construct hysteresis models from the view of electrochemical kinetics, it is a challenge to utilize these complicated models in on-board applications. This paper reviews and compares several non- electrochemical hysteresis models. Section II presents the experimental setup and test profiles. In Section III, four hysteresis models are briefly described and deeply interpreted, accompanying with the elucidation of some new findings. Furthermore, comparative simulations of these models are also demonstrated. In Section IV, by incorporating these hysteresis models into the ECM, they are verified and further compared through voltage prediction and SoC estimation on a LFPB cell. Finally, Section V summarizes and concludes this paper.

II. EQUIPMENT AND TESTS

The test bench consists of an Arbin Cycler BT2000 and its accompanying software (MITS Pro) installed on a PC, a thermal chamber, and a Matlab based simulation and

TABLE II
SPECIFICATION OF THE INVESTIGATED LFPB CELL

Chemistry	LiFePO ₄ /graphite
Rated capacity	1.1Ah@1C
Nominal voltage	3.2V
30s Max charge / discharge current	3C/10C
Upper/lower cut-off voltage	3.6V/2.2V
Nominal resistance	12mΩ

estimation algorithm run on the PC. In addition, because the current and voltage transducer accuracy of the BT2000 (0.1% FS) is not precise enough for hysteresis potential measurements, an auxiliary multimeter Fluke 8846A with a DC voltage resolution of up to 6.5-digit was employed. The specifications of the investigated 18650 cell are shown in Table II.

During tests, the cell was always under monitoring. The test procedure was interrupted or terminated when scheduled points were reached or when it was impossible to continue within equipment limits. Several tests were scheduled for OCV-SoC correlations, model parameterization and experimental verifications. Since the aim was to deliver a compact review of present popular hysteresis models and to verify their reasonability, some other concerns, e.g. aging and temperature, will be further studied in a future work. All of the data was collected on a fresh cell by containing it inside a

chamber and keeping the ambient temperature within $27 \pm 2^\circ\text{C}$.

A. OCV-SoC Correlations and Model Parameterization Test

Usually, the HPPC regime is used to establish OCV-SoC correlations and to identify ECM parameters [22], [23]. However, the instantaneous voltage drops/rebounds used to extract battery ohmic resistance are unsuitable for LFPBs since they are partially ascribed to the hysteresis potential. To acquire the OCV-SoC boundaries towards charging and discharging, i.e. $U_{oc}^{up}(z)$ and $U_{oc}^{low}(z)$, a test sequence comprising consecutive charge/discharge pulses was adopted. The maximum hysteresis potential is $V_h^{max}(z) = U_{oc}^{up}(z) - U_{oc}^{low}(z)$. Referring to [18], the values of the three electrical elements in Fig. 1(b) can be identified, i.e., deriving R_0 with the instantaneous voltage change and extracting R_p and C_p by fitting the relaxation trace. Finally, R_0 , R_p and C_p were identified as functions of the SoC during charging and discharging, respectively. The complete procedure is presented in Fig. 2(a).

B. Inner Hysteresis Trajectories Test

To explore the hysteresis mechanism, hysteresis data are indispensable. In this work, the hysteresis changing trajectories are drawn through the procedure emphasized in Fig. 2(b).

- 1) First, the cell was charged from empty to a specified SoC level of Re_{soc}^{up} (named as the reversal SoC point).
- 2) Afterwards, the cell was successively discharged with five 45s-1/3C pulses and then several 225s-1/3C pulses until the OCV went down to $U_{oc}^{low}(z)$, and the SoC was stamped as Re_r^{low} . The pulses were separated by 2h relaxations. Note that a rapid change rate of $dU_{oc}/dSoC$ was found during the initial period. Thus, the cell was first elaborately discharged with slight 45s-1/3C pulses to achieve high-resolution details of the hysteresis trajectory. Then 225s-1/3C pulses were employed to accelerate the hysteresis process since it needs a large SoC span (over 11%) to accomplish the saturated hysteresis process (from $U_{oc}^{up}(z)$ to $U_{oc}^{low}(z)$).
- 3) Another four repetitions of the above sequence were executed with Re_{soc}^{up} being equal to 45%, 60%, 75% and 90%, respectively.
- 4) To form closed hysteresis loops, the same procedure was performed from fully charged with five stamped Re_{soc}^{low} .

As a result, five hysteresis loops were drawn, as shown in Fig. 2(b).

C. Model Verification Test

For experimental verification, a simple sequence of 500s-3A alternant charge/discharge pulses and the dynamic stress

test (DST) profile were employed to evaluate the hysteresis models by comparing the predicted and measured terminal voltages. Then, to generate rich excitations, a more sophisticated dynamic profile - federal urban driving schedule (FUDS) - was used to verify the SoC estimation with the combined ECM-hysteresis models. A 240s-0.5A discharge pulse was inserted in-between the FUDS repetitions.

All the profiles were scaled to conform to the specifications in Table II and the equipment limits. As a general practice, a rest of 2h after each test was always performed prior to proceeding with further testing. This was done to allow the cell to reach an equilibrium voltage and a steady temperature.

III. HYSTERESIS MODELS

This section reviews four hysteresis models, which once validated, can be easily incorporated into ECMs and translated into mathematical expressions. Additionally, to reveal the nature of the respective models, detailed interpretations and further analysis are demonstrated, along with some improvements.

A. Geometrical Analysis Model (Model 3.1)

Marc *et al.* claimed that the hysteresis potential (V_h) depends exclusively on the charge throughput (Q_h) for NiMH batteries [23]. Then Roscher proved that this $Q_h - V_h$ relationship is applicable for LFPBs [3]. Three common scenarios portrayed in Fig. 3(a) can explain the mechanism of this model. *Scen1* ($A \rightarrow B \rightarrow A$) illustrates a normal hysteresis cycle whose terminals lie on the OCV boundaries (actually, the terminals of the spindle-shaped hysteresis loop are not exactly located on the OCV boundaries but have small offshore gaps. See **Note 4** for more details) with a charge throughput called the maximum effective hysteresis charge ($Q_{h,max}$). *Scen2* ($A \rightarrow C \rightarrow A$ or $B \rightarrow C' \rightarrow B$) delineates shallow micro-cycles with a transferred charge that is smaller than $Q_{h,max}$. *Scen3* ($A \rightarrow B \rightarrow B' \rightarrow A' \rightarrow A$) is an overflow hysteresis cycle describing the process of monotonically charging with a charge amount over $Q_{h,max}$ and then discharging to the lower boundary. The core principle is that point B is always the reference target for charging, and point A(A') is the reference target for discharging. Through experiments, it was found that the respective hysteresis semi-cycles towards charging and discharging are symmetric, and that $Q_{h,max}$ remains nearly constant for a specific battery. In *Scen1* and *Scen3*, the midpoint of the charge/discharge process ($Q_h = Q_{h,max}/2$) can be regarded as the pole of the hysteresis path. In addition, the corresponding hysteresis potential can be derived by:

$$\begin{aligned} \Delta V_{h_{mid}}^{cha}(z) &= (U_{oc}^{up}(z) - U_{oc}^{low}(z)) \times \eta_h^{cha} \\ \Delta V_{h_{mid}}^{disch}(z) &= (U_{oc}^{up}(z) - U_{oc}^{low}(z)) \times \eta_h^{disch} \end{aligned} \quad (10)$$

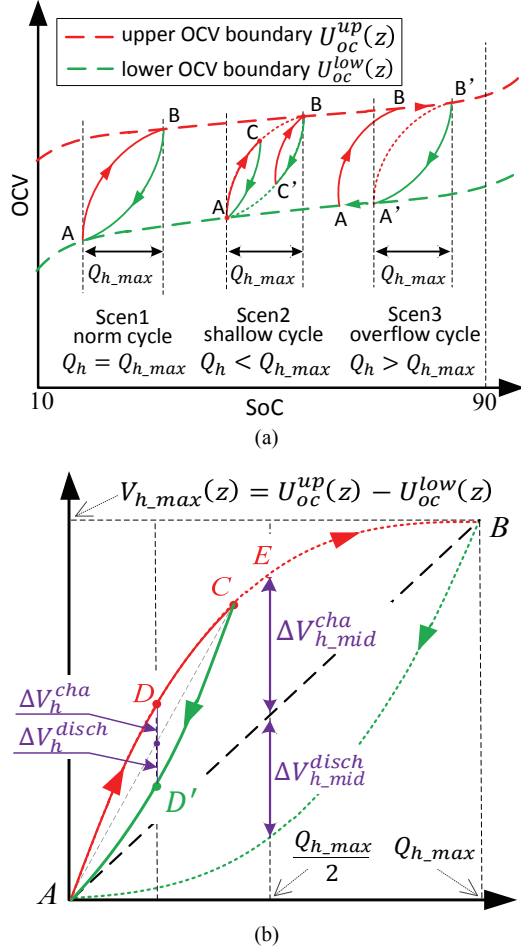


Fig. 3. Schematic illustration of the geometrical hysteresis model: (a) Three common scenarios, (b) Details of the hysteresis loop.

where η_h^{cha} and η_h^{disch} are experimentally tuned proportionality coefficients. In the case of *Scen2*, the pole D/D' of the micro-cycle ($A \rightarrow C \rightarrow A$) in Fig. 3(b) can be obtained according to relevant knowledge of geometry as:

$$\begin{aligned} \Delta V_h^{disch} &= \Delta V_{h_{mid}}^{disch} \frac{Q_h}{Q_{h_{max}}} \\ \Delta V_h^{cha} &= \Delta V_{h_{mid}}^{cha} \left(1 - \frac{Q_h}{Q_{h_{max}}}\right). \end{aligned} \quad (11)$$

Taking the shallow hysteresis cycle ($A \rightarrow C \rightarrow A$) in Fig. 3(b) as an example, when charged from the start point A on the lower OCV boundary, the corresponding target point B on the upper boundary can be determined by $SoC_B = SoC_A + Q_{h_{max}}/C_N$. C is the stochastic endpoint of the charging process. The charging trace of $A \rightarrow C$ overlaps with the normal hysteresis semi-cycle ($A \rightarrow E \rightarrow B$), which can be obtained using a spline interpolation of points A, E and B. Similarly, the discharging trajectory ($C \rightarrow D' \rightarrow A$) can be determined using C, D' and A. U_{oc} is the superimposition of the lower OCV boundary and the hysteresis voltage, i.e.:

$$U_{oc}(Q_h, z) = U_{oc}^{low}(z) + V_h(Q_h, z). \quad (12)$$

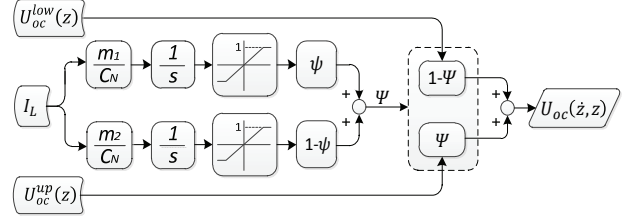


Fig. 4. Schematic illustration of the boundary-synthesis model.

B. Boundary-Synthesis Model (Model 3.2)

Without complicated mechanism analyses, an empirical black-box model was introduced to reconstruct the OCV shuttle process between the boundaries in [3]. This model uses a hysteresis factor $\Psi \in [0, 1]$, which is derived from two width factors m_1 and m_2 , two saturated current integrators and a normalization factor $\psi \in [0, 1]$ to synthesize the real-time OCV with the predetermined OCV boundaries $U_{oc}^{up}(z)$ and $U_{oc}^{low}(z)$. The structure of this model can be refined as the schematic illustrated in Fig. 4.

This model needs to be trained with experimental data to extract the parameters m_1 , m_2 and ψ . Then the model can yield the OCV as the function of the OCV boundaries and the SoC variation. In essence, this multilayered structure is analogous to the artificial neural network, and ψ , m_1 and m_2 actually act as weighting coefficients. Note that, except for the nonlinear saturation integrators, the obtained hysteresis is basically linear with the input OCV boundaries. Therefore, the outlines of the OCV boundaries primarily determine the appearance of the hysteresis trajectory.

C. Boundary-Approaching Model (Model 3.3)

Similar to Section B, Huria *et al.* put forward another boundary-framed hysteresis model [8], where the hysteresis exhibits a progressive shuttle between the OCV boundaries. The model formulation in [8] can be re-written as:

$$\frac{dU_{oc}(z)}{dz} = \begin{cases} \frac{\kappa_P (U_{oc}^{up}(z) - U_{oc}(z))}{\frac{P}{D}}, & I_L < 0 \\ \frac{\kappa_P (U_{oc}^{low}(z) - U_{oc}(z))}{\frac{P}{D}}, & I_L > 0 \end{cases} \quad (13)$$

where part D represents the derivative (change rate) of the OCV boundaries, P indicates the difference between the current point and the approaching object (boundaries), and κ_P is the convergence speed factor.

Note 2: A deep interpretation of the model in Eq. (13).

It can be concluded from Eq. (13) that part P plays an active role in diminishing the deviation between the real-time $U_{oc}(z)$ and $U_{oc}^{up}(z)/U_{oc}^{low}(z)$. Once $U_{oc}(z)$ touches the

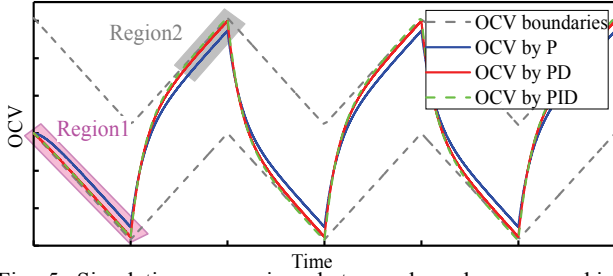


Fig. 5. Simulation comparison between boundary-approaching based hysteresis models.

boundaries, P loses efficacy and D takes responsibility for propelling $U_{oc}(z)$ to approach the boundaries by synchronizing their change rates. As a result, a feedback mechanism is formed. Inspired by the classic control law of Proportion Integration Differentiation (PID), part D in Eq. (13) can be regarded as the differential part and P can be regarded as the proportion part. It is known that the main deficiency of the PD law is the indelible static error, which has been implied in [8]. Instinctively, a reasonable adaption of Eq. (13) is the complement of the integral part as:

$$\frac{dU_{oc}(z)}{dz} = \begin{cases} \underbrace{\kappa_P (U_{oc}^{up}(z) - U_{oc}(z))}_P + \underbrace{\kappa_D dU_{oc}^{up}(z)/dz}_D + \underbrace{\kappa_I \int (U_{oc}^{up}(z) - U_{oc}(z)) dz}_I, & I_L < 0 \\ \underbrace{\kappa_P (U_{oc}^{low}(z) - U_{oc}(z))}_P + \underbrace{\kappa_D dU_{oc}^{low}(z)/dz}_D + \underbrace{\kappa_I \int (U_{oc}^{low}(z) - U_{oc}(z)) dz}_I, & I_L > 0 \end{cases} \quad (14)$$

where κ_P , κ_I and κ_D can be tuned by adjusting them to achieve the best fit with the acquired hysteresis trajectories. When compared with a PID model, the obvious disadvantages of the P and PD models can be observed from the simulation results in Fig. 5. Within the pink rectangle, the P model characterizes a sluggish response to the decline of the boundary, and the complement of part D in the PID model effectively speeds up this convergence. Within the gray rectangle, the PD model presents a static error, which is eliminated by the integral part in the PID model.

D. One-State Model (Model 3.4)

With some mathematical derivations, Plett proposed a zero-state model and a one-state model in [20], attempting to capture the hysteresis characteristic of LiBs. The zero-state model crudely simplifies the creeping hysteresis behavior as immediate flips between $U_{oc}^{up}(z)$ and $U_{oc}^{low}(z)$ rather than a slow transition like the one-state model does. The one-state model, as Eq. (15) formulates, can be operated recursively to obtain the hysteresis potential.

$$V_{h,k+1} = \mathbb{E}_{h,k} V_{h,k} + (1 - \mathbb{E}_{h,k}) \text{sign}(i_{L,k}) M_h(z_k) \quad (15)$$

where $\mathbb{E}_{h,k} = \exp(-|\gamma_k \Delta z_k|)$, $\Delta z_k = i_{L,k} \eta \Delta t / C_N$, $M_h(z_k)$ is the maximum hysteresis voltage between the boundaries, γ_k is the hysteresis rate, and both M_h and γ are assumed to be constant over the sampling period. Thereafter, the actual $U_{oc}(z)$ can be obtained from Eq. (16).

$$U_{oc}(k) = U_{oc}^{med}(k) + V_{h,k} \quad (16)$$

In [20], Plett developed an EKF-based approach to parameterize M_h and γ , which are correlated with the SoC, i.e., $M_h(z)$ and $\gamma(z)$. In [24], a complicated meta-heuristic teaching-learning method was employed to search for the optimal values of γ and M_h , which were deemed as constants across the entire SoC range.

Note 3: An efficient and simple approach for the identification of γ and M_h .

Eq. (15) can be expressed in continuous-time field as:

$$V_h(t) = V_h^\infty + (V_h^0 - V_h^\infty) \exp(-|\Delta z_k|/\tau_h) \quad (17)$$

where $V_h(t) = V_{h,k+1}$, $V_h^0 = V_{h,k}$, $V_h^\infty = \text{sign}(i_{L,k}) \cdot M_h$ and $\tau_h = 1/\gamma$. Eq. (17) is similar to the time response expression of the first-order circuit. Therefore, τ_h can be regarded as a pseudo “time constant” regarding the SoC as the actuating quantity. Through exploring the hysteresis trajectories acquired in Fig. 2(b), the initial ($t = 0$), the steady ($t = \infty$) states and τ_h can be easily fitted. Thereby, an easier way is developed to extract M_h and τ_h . The vertical distance (ΔV) between the terminals of a hysteresis loop can be regarded as $2M_h$, and τ_h can be obtained by fitting the trajectory as an exponential.

However, there is an obvious discrepancy between the outer OCV boundaries and the inner hysteresis loops, which is inconsistent with the assumption as mentioned above.

Note 4: Why are not the terminals of hysteresis loops just located on the OCV boundaries?

As illustrated in **Note 3**, hysteresis evolution is approximated as an exponential response of first-order circuits regarding the charge throughput (Q_h) as the action quantity. It is known that the exponential function shows a drastic change during the initial period. This means that a tiny charge throughput (ΔQ_{tiny}) can lead to a significant hysteresis potential (ΔOCV_{inst}) burst away from the boundaries, as delineated in Fig. 6(a). Since it is difficult to control the charge throughput slightly with steps small enough ($\Delta Q_h < \Delta Q_{tiny}$), an immediate jump from the OCV boundaries can usually be observed, which results in isolated inner loops. Consequently, it is reasonable to speculate that a more complete and accurate hysteresis cycle can be reshaped by pushing the semi-cycles at an opposite displacement as Fig. 6 (b) illustrates.

Due to complex electrochemical reactions, battery behaviors contain both short-time and long-time details, which can

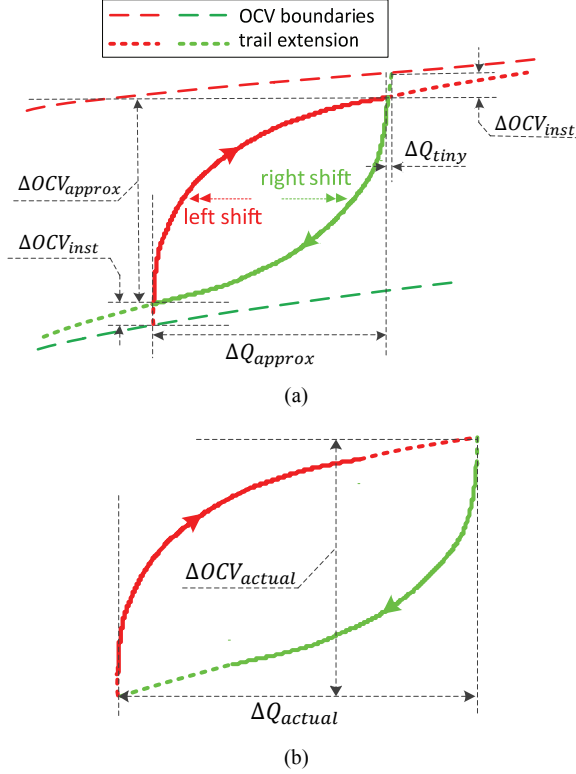


Fig. 6. Schematic illustration of the offshore gaps of the hysteresis loop: (a) Mechanism analysis, (b) The complete hysteresis loop.

hardly be accommodated meticulously by the one-state model with just an exponential term. To adapt the one-state model, an instantaneous OCV drop/rise (the ΔOCV_{inst} in Fig. 6) is incorporated as:

$$V_h(k+1) = \exp(-|\gamma(k)\Delta z(k)|)V_h(k) + (1 - \exp(-|\gamma(k)\Delta z(k)|))\text{sign}(i(k))M_h(k) + \Delta OCV_{inst}\lambda(k) \quad (18)$$

$$\text{where } \lambda(k) = \begin{cases} \text{sign}(i(k)), & \text{sign}(i(k)i(k-1)) = -1 \\ 0, & \text{otherwise} \end{cases}$$

E. Simulation Comparison between the Hysteresis Models

In order to investigate the working mechanisms of the four discussed hysteresis models, simulations are conducted in MATLAB. The OCV boundaries are assumed to be parallel inclined straight lines to simplify the simulation. First, 500s charge/discharge pulses are applied, whereby saturated hysteresis can be achieved. As can be seen in Fig. 7(a), the OCVs produced by the four models can reach the boundaries in nearly 160s. Model 3.1 gives a gentle approaching process. The OCV of Model 3.2 emphasizes distinct corners as implied in Section 3.2. Models 3.3 and 3.4 have nearly the same OCV outlines and a rapid upspring can be expected over the initial short period. Then 5s charge/discharge pulses are applied. As depicted in Fig. 7(b), some interesting phenomena occur. When the pulse number increases, the OCVs of Models 3.1 and 3.2 creep around the lower

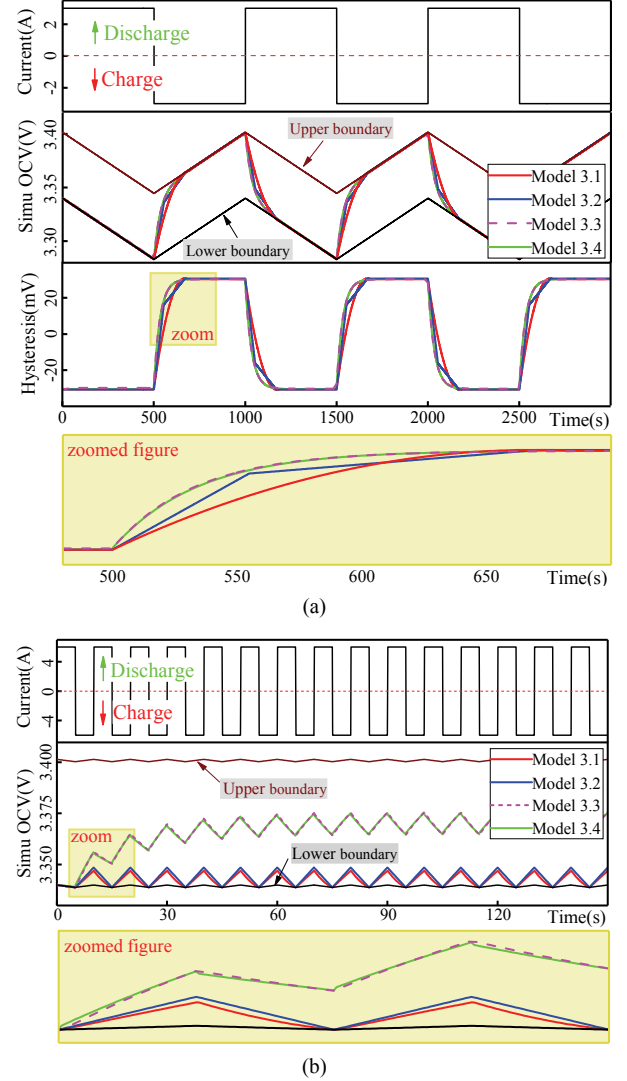


Fig. 7. Simulation comparison between the four hysteresis models described in Section III. A, B, C and D, by applying: (a) 500s charge/discharge pulses, (b) 5s charge/discharge pulses.

TABLE III
CONSUMED TIMES OF THE RESPECTIVE HYSTERESIS MODELS FOR 10000 CALCULATIONS.

Model	Consumed time (ms)
Model 3.1	565.3
Model 3.2	26.5
Model 3.3	41.7
Model 3.4	81.0

boundary, induced by the small, back and forth charge throughputs. However, Models 3.3 and 3.4 produce slowly climbing OCVs. The rationality for these models needs to be further discerned by experiments in next section.

Computational burden is a non-negligible concern for on-board applications. Ten thousand calculations of every model are operated on the PC (Core i3-3220, 3.3 GHz) and the consumed times are listed in Table III. Obviously, in

terms of algorithm complexity, Model 3.1 gives the worst performance, followed by Model 3.4, which, however, is much more time-saving than Model 3.1. The most efficient model is Model 3.2, while Model 3.3 is also competitive.

IV. EXPERIMENTAL VERIFICATION

This section arranges several experiments to present a comprehensive comparison on the four hysteresis models in terms of terminal voltage prediction and SoC estimation. The parameters of the models are extracted from the acquired data in Section 2. Since high-rate currents can incur unexpected side reactions and inspire nonlinear distortions, the peaks of the simple sequence were scaled to 3A, the DST sequence to 5A, and the FUDS sequence to 2A.

A. Terminal Voltage Prediction

First, the simple current sequence in Fig. 7(a) was applied on the cell. The measured terminal voltages were compared with the simulated terminal voltages (calculated by the ECM-hysteresis models) in Fig. 8(a). It can be seen that all four models can closely track the real voltage responses. Then the DST sequence, which contains more dynamics, was played. From Fig. 8(b), it can be seen that as the number of pulses increases, rising deviations can be observed on Models 3.3 and 3.4, whereas Models 3.1 and 3.2 produce relatively high-quality outputs. Terminal voltage prediction experiments show good agreement with the simulations in Section III. E.

B. SoC Estimation

Then the previously formulated EKF-based SoC estimation algorithm was executed under the FUDS profile and the result is exhibited in Fig. 8(c). Since an Ah counting operation is incorporated into Eq. (2), an accumulated error is inevitable. However, the error evolutions of Models 3.3 and 3.4 characterize a steep climb during the initial short period (the cyan ellipse). Thereafter, they keep a relatively constant difference from the errors of Models 3.1 and 3.2. When subject to a long-time discharge, the errors of Models 3.3 and 3.4 experience noticeable convergence (the yellow ellipses).

Relevant performance indexes of the four hysteresis models for voltage predication and SoC estimation are tabulated in Table IV. Although Models 3.3 and 3.4 have been improved, the defects of their mechanisms restrict the room for performance improvement. During the high dynamic experiment of Fig. 8(b), Models 3.1 and 3.2 exhibit mean errors that are much smaller than the errors of Models 3.3 and 3.4. For the SoC estimation experiment, results suggest that Models 3.1 and 3.2 once again surpass Models 3.3 and 3.4. To sum up, Models 3.1 and 3.2 can provide better hysteresis reproductions than Models 3.3 and 3.4.

Note 5: Why do Models 3.3 and 3.4 suffer gradually rising errors, in contrast to Models 3.1 and 3.2?

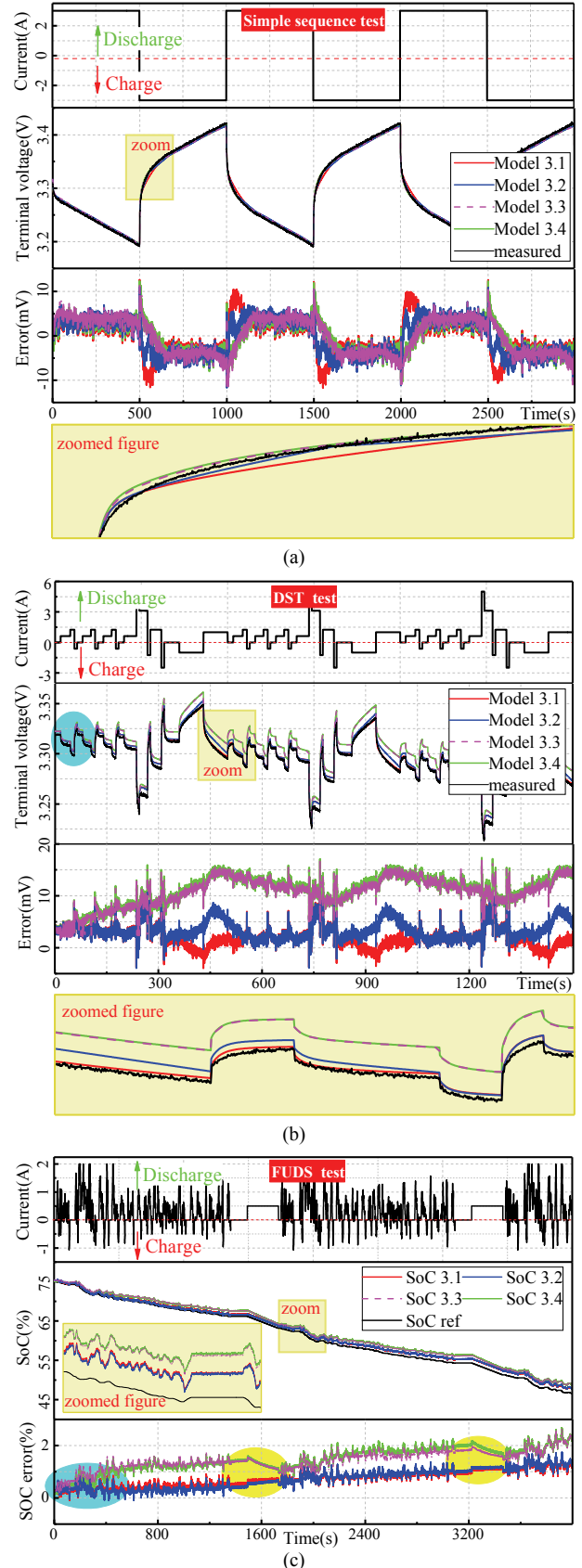


Fig. 8. Experimental comparisons of the four hysteresis models through voltage predictions with: (a) Simple sequence, (b) DST sequence, (c) SoC estimation with the FUDS profile.

TABLE IV
PERFORMANCE OF THE 4 HYSTERESIS MODELS FOR TERMINAL
VOLTAGE PREDICTION AND SOC ESTIMATION

Model	Voltage prediction abs error in Fig.8 (a)/(b)		
	Mean (mV)	Max (mV)	Variance(10^{-6})
3.1	3.6/2.4	13.6/11.1	3.1/2.9
3.2	3.8/3.5	11.6/11.7	1.2/3.1
3.3	3.7/10.8	11.8/18.9	1.8/8.0
3.4	3.3/11.0	13.3/19.1	1.4/8.2
Model	SoC estimation abs error Fig.8 (c)		
	Mean (%)	Max (%)	Variance(10^{-2})
3.1	0.87	1.72	13.7
3.2	0.89	1.86	20.6
3.3	1.65	2.78	25.6
3.4	1.69	2.84	32.4

Taking the evolution from the lower boundary upwards to the upper boundary as an example:

- 1) For Model 3.1, the hysteresis trajectory proceeds along an arc-shaped path. The core principle that V_h is proportional to Q_h is consistent with the electrochemical essence of hysteresis. Model 3.2 has a network structure and similar abilities to artificial neural networks. Using parameters extracted from actual data, Model 3.2 can guarantee the basic accuracy for complex correlation approximation. Therefore, a relatively reliable result can be achieved. However, it gives a switch corner halfway the transition, as suggested by simulations (Fig. 7(a)) and experiments (Fig. 8(a)).
- 2) For Models 3.3 and 3.4, the climbing rate is determined by and proportional to the difference between the present point and the target boundary. Accordingly, the initial period has the largest changing rate, and subsequently, the rate reduces gradually. Therefore, when approaching the upwards direction and the downwards direction from a specific point, this mechanism gives asymmetric rates, especially for points near the boundaries. As a result, when successive charge and discharge pulses are applied with the same amount of charge, the response characterizes a rapid climb first, then a sluggish descent, which results in an absolute upwards displacement.

V. DISCUSSION AND CONCLUSIONS

To deal with the troublesome hysteresis potential of LFPBs, this paper lists four elaborate hysteresis models. Furthermore, some deep interpretations and new findings are demonstrated.

- 1) Model 3.1 holds a core principle that the hysteresis potential is quantitatively correlated with the charge throughput. On the basis of this principle, a hysteresis

model is established geometrically.

- 2) Model 3.2 is essentially similar to the structure of the artificial neural network (ANN). Without complicated mechanism analyses, a simple pseudo-ANN is structured to emulate a battery.
- 3) Model 3.3 refers to the thought of PD control law. Due to the lack of an integral part, static errors are inevitable. Therefore, the integral part is complemented to make the model more flexible by adding two tunable coefficients.
- 4) Model 3.4 approximates the hysteresis process as a first-order circuit response. Since real hysteresis behavior is complicated and contains multi-order details, an instantaneous change part is added to this model to capture the initial short-time behavior.

These models have concise mathematical expressions and can be conveniently incorporated into ECMs. Three levels of comparisons have been performed on these models.

- 1) Simulation comparison. In Section III. E, simulations were performed to preliminarily evaluate these models, and to verify their differences as analyzed in Section III. A-D.
- 2) Experimental comparison. In Section IV. A, experiments on voltage prediction, which is a direct performance index of hysteresis reproducing, are conducted.
- 3) Application comparison. Accurate battery models are crucial for SoC estimation, power ability perdition and battery string energy equalization. In Section IV. B, these hysteresis models were applied to general SoC estimation.

Through comprehensive simulation and experiment comparisons, it can be seen that Models 3.1 and 3.2 provide better accuracy than Models 3.3 and 3.4. However, Model 3.1 is the most time-consuming model. Considering both complexity and model accuracy, it is reasonable to conclude that Model 3.2 is superior to Models 3.1, 3.3 and 3.4.

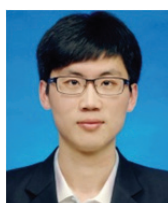
REFERENCES

- [1] M. Safari and C. Delacourt, "Aging of a commercial graphite/LiFePO₄ cell," *J. The Electrochemical Society*, Vol. 158, No. 10, pp. A1123-A1135, Dec. 2011.
- [2] O. K. Park, Y. Cho, S. Lee, H. C. Yoo, H. K. Song, and J. Cho, "Who will drive electric vehicles, olivine or spinel?" *Energy & Environmental Science*, Vol. 4, No. 5, pp. 1621-1633, Apr. 2011.
- [3] M. A. Roscher and D. U. Sauer, "Dynamic electric behavior and open-circuit-voltage modeling of LiFePO₄-based lithium ion secondary batteries," *J. Power Sources*, Vol. 196, No. 1, pp. 331-336, Jan. 2011.
- [4] S. Nejad, D. T. Gladwin, and D. A. Stone, "A systematic review of lumped-parameter equivalent circuit models for real-time estimation of lithium-ion battery states," *J. Power Sources*, Vol. 316, pp. 183-196, Jun. 2016.

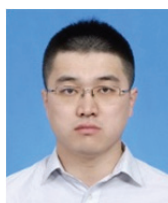
- [5] A. Hausmann and C. Depcik, "Expanding the Peukert equation for battery capacity modeling through inclusion of a temperature dependency," *J. Power Sources*, Vol. 235, pp. 148-158, Aug. 2013.
- [6] J. Li, J. K. Barillas, C. Guenther, and M. A. Danzer, "A comparative study of state of charge estimation algorithms for LiFePO₄ batteries used in electric vehicles," *J. Power Sources*, Vol. 230, pp. 244-250, May 2013.
- [7] Z. Wei, T. M. Lim, M. Skyllas-Kazacos, N. Wai, and K. J. Tseng, "Online state of charge and model parameter co-estimation based on a novel multi-timescale estimator for vanadium redox flow battery," *Applied Energy*, Vol. 172, pp. 169-179, Jun. 2016.
- [8] T. Huria, G. Ludovici, and G. Lutzemberger, "State of charge estimation of high power lithium iron phosphate cells," *J. Power Sources*, Vol. 249, pp. 92-102, Aug. 2014.
- [9] W. Waag, C. Fleischer, and D. U. Sauer, "Critical review of the methods for monitoring of lithium-ion batteries in electric and hybrid vehicles," *J. Power Sources*, Vol. 258, pp. 321-339, Jul. 2014.
- [10] Z. Wei, S. Meng, K. J. Tseng, T. M. Lim, B. H. Soong, and M. Skyllas-Kazacos, "An adaptive model for vanadium redox flow battery and its application for online peak power estimation," *J. Power Sources*, Vol. 344, pp. 195-207, Mar. 2017.
- [11] V. Pop, H. J. Bergveld, J. H. G. Op het Veld, P. P. L. Regtien, D. Danilov, and P. H. L. Notten, "Modeling battery behavior for accurate state-of-charge indication," *J. The Electrochemical Society*, Vol. 153, No. 11, pp. A2013-A2022, Sep. 2006.
- [12] M. A. Roscher, O. Bohlen, and J. Vetter, "OCV hysteresis in Li-ion batteries including two-phase transition materials," *Int. J. Electrochemistry*, Vol. 2011, Feb. 2011.
- [13] J. B. Gerschler and D. U. Sauer, "Investigation of open-circuit-voltage behaviour of lithium-ion batteries with various cathode materials under special consideration of voltage equalisation phenomena," *In EVS24 International Battery, Hybrid and Fuel Cell Electric Vehicle Symposium*, 2009.
- [14] A. Farmann, W. Waag, A. Marongiu, and D. U. Sauer, "Critical review of on-board capacity estimation techniques for lithium-ion batteries in electric and hybrid electric vehicles," *J. Power Sources*, Vol. 281, pp. 114-130, May 2015.
- [15] L. Lu, X. Han, J. Li, J. Hua, and M. Ouyang, "A review on the key issues for lithium-ion battery management in electric vehicles," *J. Power Sources*, Vol. 226, pp. 272-288, Mar. 2013.
- [16] G. Dong, J. Wei, and Z. Chen, "Kalman filter for onboard state of charge estimation and peak power capability analysis of lithium-ion batteries," *J. Power Sources*, Vol. 328, pp. 615-626, Oct. 2016.
- [17] G. L. Plett, "Extended Kalman filtering for battery management systems of LiPB-based HEV battery packs: Part 3. State and parameter estimation," *J. Power Sources*, Vol. 134, No. 2, pp. 277-292, Aug. 2004.
- [18] F. Sun, R. Xiong, H. He, W. Li, and J. E. E. Aussems, "Model-based dynamic multi-parameter method for peak power estimation of lithium-ion batteries," *Applied Energy*, Vol. 96, pp. 378-386, Aug. 2012.
- [19] R. Xiong, X. Gong, C. C. Mi, and F. Sun, "A robust state-of-charge estimator for multiple types of lithium-ion batteries using adaptive extended Kalman filter," *J. Power Sources*, Vol. 243, pp. 805-816, Dec. 2013.
- [20] G. L. Plett, "Extended Kalman filtering for battery management systems of LiPB-based HEV battery packs: Part 2. Modeling and identification," *J. Power Sources*, Vol. 134, No. 2, pp. 262-276, Aug. 2004.
- [21] H. Konishi, T. Hirano, D. Takamatsu, A. Gunji, X. Feng, and S. Furutsuki, "Origin of hysteresis between charge and discharge processes in lithium-rich layer-structured cathode material for lithium-ion battery," *J. Power Sources*, Vol. 298, pp. 144-149, Dec. 2015.
- [22] J. P. Christopherson, "Battery test manual for electric vehicles," Idaho National Laboratory, 2015.
- [23] M. Thele, O. Bohlen, D. U. Sauer, and E. Karden, "Development of a voltage-behavior model for NiMH batteries using an impedance-based modeling concept," *J. Power Sources*, Vol. 175, No. 1, pp. 635-643, Jan. 2008.
- [24] C. Zhang, K. Li, L. Pei, and C. Zhu, "An integrated approach for real-time model-based state-of-charge estimation of lithium-ion batteries," *J. Power Sources*, Vol. 283, pp. 24-36, Jun. 2015.



Jiachen Ma was born in China, in 1964. He received his B.S., M.S. and Ph.D. degrees in Control Science and Engineering from the Harbin Institute of Technology, Harbin, China, in 1985, 1988 and 2006, respectively. He is presently working as a Professor in the School of Astronautics, Harbin Institute of Technology. His current research interests include intelligent robots, precise machine vision detection, embedded systems and applications, and battery energy management.



Jiale Xie received his B.S. degree from the Harbin Engineering University, Harbin, China, in 2010; and his M.S. degree in Control Science and Engineering from the Harbin Institute of Technology, Harbin, China, in 2012, where he is presently working towards his Ph.D. degree in the School of Astronautics. From 2012 to 2013, he worked for the Envision Energy Co., Ltd., Shanghai, China, where he was in charge of control strategies for wind turbines. His current research interests include battery modeling and simulation, states estimation of power Li-ion batteries, series battery string equalization and embedded control.



Kun Bai received his B.S. and M.S. degrees in Control Science and Engineering from the Harbin Engineering University, Harbin, China, in 2010 and 2013, respectively. Since 2013, he has been working at the Maintenance Branch of the State Grid Jibei Electric Power Co. Ltd., Beijing, China, where he is in charge of power grid failure diagnosis. His current research interests include high-voltage insulation, smart power grids and wind-solar-storage hybrid power systems.